RESEARCH ARTICLE

Macromolecular Rapid Communications
www.mrc-journal.de

Porous Anisometric PNIPAM Microgels: Tailored Porous Structure and Thermal Response

*Lea Steinbeck, Hanna J. M. Wolff, Maximilian Middeldorf, John Linkhorst, and Matthias Wessling**

The porous structure of microgels significantly influences their properties and, thus, their suitability for various applications, in particular as building blocks for tissue scaffolds. Porosity is one of the crucial features for microgel–cell interactions and significantly increases the cells' accumulation and proliferation. Consequently, tailoring the porosity of microgels in an effortless way is important but still challenging, especially for nonspherical microgels. This work presents a straightforward procedure to fabricate complex-shaped poly(*N*-isopropyl acrylamide) (PNIPAM) microgels with tuned porous structures using the so-called cononsolvency effect during microgel polymerization. Therefore, the classical solvent in the reaction solution is exchanged from water to water–methanol mixtures in a stop-flow lithography process. For cylindrical microgels with a higher methanol content during fabrication, a greater degree of collapsing is observed, and their aspect ratio increases. Furthermore, the collapsing and swelling velocities change with the methanol content, indicating a modified porous structure, which is confirmed by electron microscopy micrographs. Furthermore, swelling patterns of the microgel variants occur during cooling, revealing their thermal response as a highly heterogeneous process. These results show a novel procedure to fabricate PNIPAM microgels of any elongated 2D shape with tailored porous structure and thermoresponsiveness by introducing the cononsolvency effect during stop-flow lithography polymerization.

1. Introduction

Microgels have developed from model colloids to building blocks for new material systems with various applications.[1] They are highly swollen polymer networks and have an internal gel-like structure. Microgels provide several beneficial properties, such as being stimuli sensitive to temperature, pH, and ionic strength, and even being biocompatible.[2–4] Their softness and interfaces can be engineered[5] to tailor them, for instance, for cell seeding and cell proliferation. These properties enable the application of microgels as building blocks for minimally invasive scaffolds in tissue engineering.[6–12] Anisometric shapes of the microgels further enhance cell infiltration, migration, and proliferation within these scaffolds.[12–16] Thereby, internal pores in the nanometer scale inside the microgels significantly influence the microgels' functionality and application possibilities.[17–23] These internal pores enable nutrient supply[24] or loading and protective surrounding of drugs.[25] These effects are not only caused by different ratios of void volume to total volume as per the classical definition of porosity. Besides this, characteristics such as the tortuosity, the sphericality or shape of the pores, the pore size distribution, the texture of the polymeric network, or its directionality must be considered when analyzing the porosity, or more accurately, the porous structure of microgels. Furthermore, this porous structure is directly related to the mechanical properties of the microgels as cell support, which has been investigated as one major influencing parameter on cell behavior, especially concerning growth, adhesion, and differentiation.[21,26–28] Hence, internal pores play a major role in the success of microgels as biomedical scaffolds. Furthermore, a high porosity results in a high surface area, and thus, a faster response to external stimuli.[17,29] Microgels respond to various stimuli such as pH, ionic strength, or in the case of poly(*N*-isopropyl acrylamide) (PNIPAM) temperature, changing their volume and shape and, in turn, their mechanical properties.[3,4,30,31] These temperature-dependent changes of microgels enable further advantages such as controlled drug release,[2,25] enhanced imitation of the active and dynamic cell environment,[32] regulated cell training, or cell harvesting.[3]

L. Steinbeck, H. J. M. Wolff, M. Middeldorf, J. Linkhorst[+], M. Wessling
Chemical Process Engineering (AVT.CVT)
RWTH Aachen University
Forckenbeckstraße 51, 52074 Aachen, Germany
E-mail: manuscripts.cvt@avt.rwth-aachen.de

M. Wessling
DWI – Leibniz-Institute for Interactive Materials
Forckenbeckstraße 50, 52074 Aachen, Germany

The ORCID identification number(s) for the author(s) of this article can be found under https://doi.org/10.1002/marc.202300680

[+]Present address: Process Engineering of Electrochemical Systems, Technical University of Darmstadt, Otto-Berndt-Str. 2, 64287 Darmstadt, Germany

DOI: 10.1002/marc.202300680

Besides applications in biomedical science, the porosity of hydrogels is important for various other applications and is of interest in many topics like agriculture, membrane separation processes, or catalysts.[33]

The thermal response of the microgels is reversible, but collapsing and swelling differ in the case of PNIPAM and related polymers, revealing a hysteresis. The individual polymer chain interactions are temperature-dependent and behave differently for the same temperature values during collapsing, in contrast to swelling. Slightly below the lower critical solution temperature (LCST), some inter- and intrachain hydrogen bonds remain during the swelling process, which are not present during the collapsing at the same temperatures. Furthermore, the microgels' shells swell more than their cores during swelling. The resulting inhomogeneous swelling of microgels allows to further achieve areas of varying density and aggregation within one microgel during the microgel's thermal response.[34–37] Thus, pores within microgels are directly related to the functionality, mechanical properties, biocompatibility, and responsiveness of microgels. This provides a broad field of applications and a desired need to adapt these internal pores. However, a simple and efficient variation of the porosity within microgels remains challenging, especially with respect to anisometric microgels.

The porous structure and softness of microgels are generally adjusted by changing the amount of monomer or cross-linker as essential chemical components in the reaction solution.[30,38–40] For UV-initiated radical polymerization, the variation of the exposure time and the radiant flux is carried out for this purpose.[41] However, these options allow limited flexibility only. Hence, methods to selectively introduce pores into microgels, change their pore shapes, or their polymeric structure without changing their chemical composition are of particular interest.[33] One simple and often applied method is to use templates for the pores during the synthesis.[17–21,25] In the case of PNIPAM microgels, oil droplets[17] and solid particles[25] are used as templates in the reaction solution for droplet polymerization. Also, gas bubbles[19] and porogens[20,21,42,43] are applied as templates in porous particle synthesis. In addition to templates, in microgel synthesis, porosity can also be induced or adapted using the cononsolvency effect for bulk hydrogels,[22,23] hybrid gels,[44] or microspheres.[18] The cononsolvency effect appears with PNIPAM polymers when dissolved in mixtures of two distinct good solvents, such as water and methanol. The polymer is swollen in each pure phase, water or alcohol, but collapses in mixtures of both.[31,45–47] Competitive hydrogen bonding of water and methanol to the polymer chains of PNIPAM results in a conformation change of these chains and thus in the cononsolvency effect.[45,48,49] The strongest collapse of spherical PNIPAM microgels is described for a methanol mole fraction of ≈0.15–0.2. During this cononsolvency-induced collapse, methanol enriches inside the PNIPAM gels.[23,47,50] Instead of only observing the cononsolvency effect on polymers after fabrication, the effect can be used directly during hydrogel synthesis. Thus, PNIPAM microgels with an altered porous structure are formed without the need for the dispersion of templates in the reaction solution or an additional step to dissolve the solid templates from the pores.[22,23,44] This approach is reported for spherical microgels fabricated via precipitation or emulsion polymerization but lacks a transfer to light-induced radical polymerization via projection lithography and anisometric microgels, which are among others favorable for cell culture scaffolds.[12–16] Using fabrication techniques like projection lithography, any desired elongated 2D shape of microgels is possible. This freedom in microgel shape enables benefits in various applications, like in the field of biomedical science, allowing to generate injectable scaffolds for cell growth with tailored scaffold properties on various length scales.[4,51–54] Furthermore, light-induced polymerization enables a greater ability to tune the microgels due to the flexibility of the fabrication method.

In this work, the effect of methanol on the porous structure and the responsiveness of anisometric PNIPAM microgels is investigated using stop-flow lithography (SFL) as a fabrication technique. Specifically, rod-shaped microgels are investigated. However, the presented procedure can be used to fabricate any desired microgel shape in future works, revealing the possibility of variation of the fabricated microgels and their wide range of applications. To tailor the porous structure by the control of the cononsolvency effect, the water content in the reaction solution for PNIPAM microgels is partly replaced with methanol, starting from the standard NIPAM solution containing 20 wt% NIPAM, 2 wt% N, N'-methylene bisacrylamide (BIS), 1 wt% lithium phenyl-2,4,6-trimethylbenzoylphosphinate (LAP), and 40 mmol L^{-1} sodium dodecyl sulfate (SDS)-water as solvent. Microgels are fabricated with varying amounts of methanol between 0 and 50 wt%, and the respective fabrication parameters applied are investigated. The porosity and polymeric structure of the microgels are qualitatively and quantitatively determined by high-resolution electron microscopy with a subsequent software-based evaluation and by comparing the velocity of the thermal responsiveness of the microgels. Moreover, the outer appearance, the collapsed and swollen states, and the overall thermal behavior of the microgels are observed by light microscopy, allowing further analysis of swelling patterns as a function of the methanol content.

2. Results and Discussion

2.1. Microgel Fabrication during SFL

To adapt the porous structure and softness of anisometric microgels, the cononsolvency effect is used during microgel synthesis by stop-flow lithography (SFL). More radiant energy is needed in the presence of methanol to form stable microgels, which is shown in Figure S1 (Supporting Information). This observation indicates that polymerization proceeds less efficiently in a water–methanol mixture. The polymerization induced in this work is based on two different effects: the light-induced radical polymerization via projection lithography and the polymerization in the presence of a cononsolvent. Separately, both effects are described in the literature. Dendukuri et al.[55] model the light-induced free radical polymerization of microgels occurring inside microfluidic devices out of polydimethylsiloxane (PDMS). Here, the four stages of radical polymerization are described, namely, photolysis, chain initiation, chain propagation, and chain termination. The fifth possible reaction provides the inhibition of the polymer reaction via oxygen. This reaction mechanism can be directly transferred to the polymer reaction considered in this study. However, if methanol is added to the reaction solution, the cononsolvency effect influences the polymer formation. This influence so far is only described for spherical microgels during precipitation polymerization.[22,23,44] Here, the observed differences in the microgels are related to the collapse of the PNIPAM chain segments due to their decreased solubility during formation inside the alcohol-water mixture. However, the chemical composition of the microgels is not affected by the cononsolvency effect during fabrication and, thus, remains the same despite the methanol content in the reaction solution.[23] The polymer conversion in this work is determined by both described literature effects, light-induced radical polymerization and cononsolvency-induced phase separation, leading to more radiant energy being needed for microgel formation in a cononsolvent. Whereas the same polymerization conditions could be used for the fabrication of microgels with methanol contents of 0–40 wt%, no stable microgels could be fabricated in a reaction solution of 50 wt% methanol with these parameters. Consequently, the exposure time was increased to successfully form microgels in 50 wt% methanol, making them theoretically stiffer than the other microgel variants. On the contrary, the microgels get more deformable with increasing methanol content, as visually observed during the flow period of the SFL process. Furthermore, their post-swelling within the fabrication channel intensifies, exceeding the channel height. Thus, varying methanol contents in the reaction solution affect the properties of gels formed during the SFL process and will be analyzed in detail in the following subsections.

2.2. Methanol-Dependent Microgel Dimensions

The optical appearance of the microgels was investigated by brightfield micrographs shown in **Figure** 1a. These micrographs show the optical appearance and contour of the microgels in the swollen and collapsed state, respectively. The more collapsed a microgel is, the better its contours are visible since the refractive index increases. For an increasing methanol content, the microgel length increases in the swollen state and decreases in the collapsed state. Furthermore, especially the 40 and 50 wt% microgels are more elongated than the variants fabricated with less methanol, showing the dependence of the aspect ratio on the methanol content in both states, swollen and collapsed.

To quantify the observed qualitative observation, the microgel lengths and widths were evaluated at low and high temperatures to compare the microgels in the swollen (22 °C) and collapsed (40 °C) state depending on their methanol content. The cleaning of the microgel samples prior to analysis is conducted via dialysis. This procedure is commonly reported to remove short polymer chain fragments from microgels.[56,57] If highly water-soluble polymer chains would still remain after cleaning, these would, at most, hinder rather than intensify the microgels' collapsing and swelling.[56] Consequently, these potentially remaining polymer chains will not be considered in further discussions. Figure 1b shows the microgel length in the swollen, respectively collapsed, state as a function of the methanol content during fabrication. Both curves, swollen and collapsed, show a distinct trend with increasing methanol content. The curves start to significantly diverge at 20 wt% methanol. At this point, the size of the swollen microgels increases, whereas that of the collapsed microgels decreases. The swollen microgels fabricated in the presence of 50 wt% methanol are 56% ± 5% larger than microgels fabricated without methanol, whereas the same 50 wt% sample is 27% ± 4% smaller in the collapsed state. The blue shaded area in Figure 1b demonstrates the increase in the length difference of both states for higher methanol content. Due to 50 wt% methanol, the collapsing degree increases to 76% ± 13% in comparison to 49% ± 4% for the methanol-free sample (compare Figure S3a and Table S1, Supporting Information). Thus, methanol has a significant influence on the collapsing degree of the thermoresponsive microgels. Independent of the methanol content, all microgels in their swollen state exceed the channel height of 80 µm. Hence, the microgels swell after the SFL fabrication, resulting from the exchange of the reaction solution against water after fabrication. The water used during the collapsing and swelling experiments lacks those chemicals present in the reaction solution, resulting in different osmotic contributions. Thus, osmotic deswelling in the SFL channel causes a greater length of the microgels than the channel height after fabrication. The difference between the osmotic conditions of the reaction solution composition and the experimental swelling/collapse solution even increases with higher methanol contents. Thus, the post-swelling intensifies with an increase in the methanol content because of two reasons: a) the difference in the solutions and b) the microgel properties themselves.

In addition to the lengths of the microgels, their widths during collapsing and swelling were investigated (compare Figure S3b and Table S2, Supporting Information). Dividing the length by the width of the microgel yields the aspect ratio, which illustrates the shape-related collapsing and swelling. Figure 1c shows the aspect ratio of the swollen and collapsed states as a function of the methanol content in the reaction solution during fabrication. The aspect ratio of the rod-shaped microgels depends on the methanol content in both the swollen and the collapsed states. Up to 30 wt% methanol, the aspect ratios of all samples remain constant at 3. Subsequently, with increasing methanol content to 40 and 50 wt% methanol, the aspect ratio significantly increases, resulting in the lengths of the microgels being up to six times their widths. Thus, microgels are thinner and more elongated if a higher methanol content is present during fabrication. The aspect ratios are consistent between the swollen and the collapsed state of each microgel sample, except for the sample with 50 wt% methanol. However, this sample has comparatively large errors, with the difference between the swollen and collapsed state being within the error range.

The observed increased degree of collapsing with a higher methanol content enables a broadened collapsing window in the microgels' response to external stimuli. For future applications, this extended response may proof beneficial to provide a stimulus in cellular environments or through higher drug loading.

2.3. Visual Analysis of the Polymeric Microgel Network

Microgel samples were sublimated (cryo) to remove solvent from the swollen microgel and to image the remaining polymer features using field emission scanning electron microscopy (FE-SEM). The micrographs in **Figure** 2a,b provide an indication of their polymeric structure (see also Figure S6, Supporting Information, for more micrographs). The 0 and 40 wt% variants are

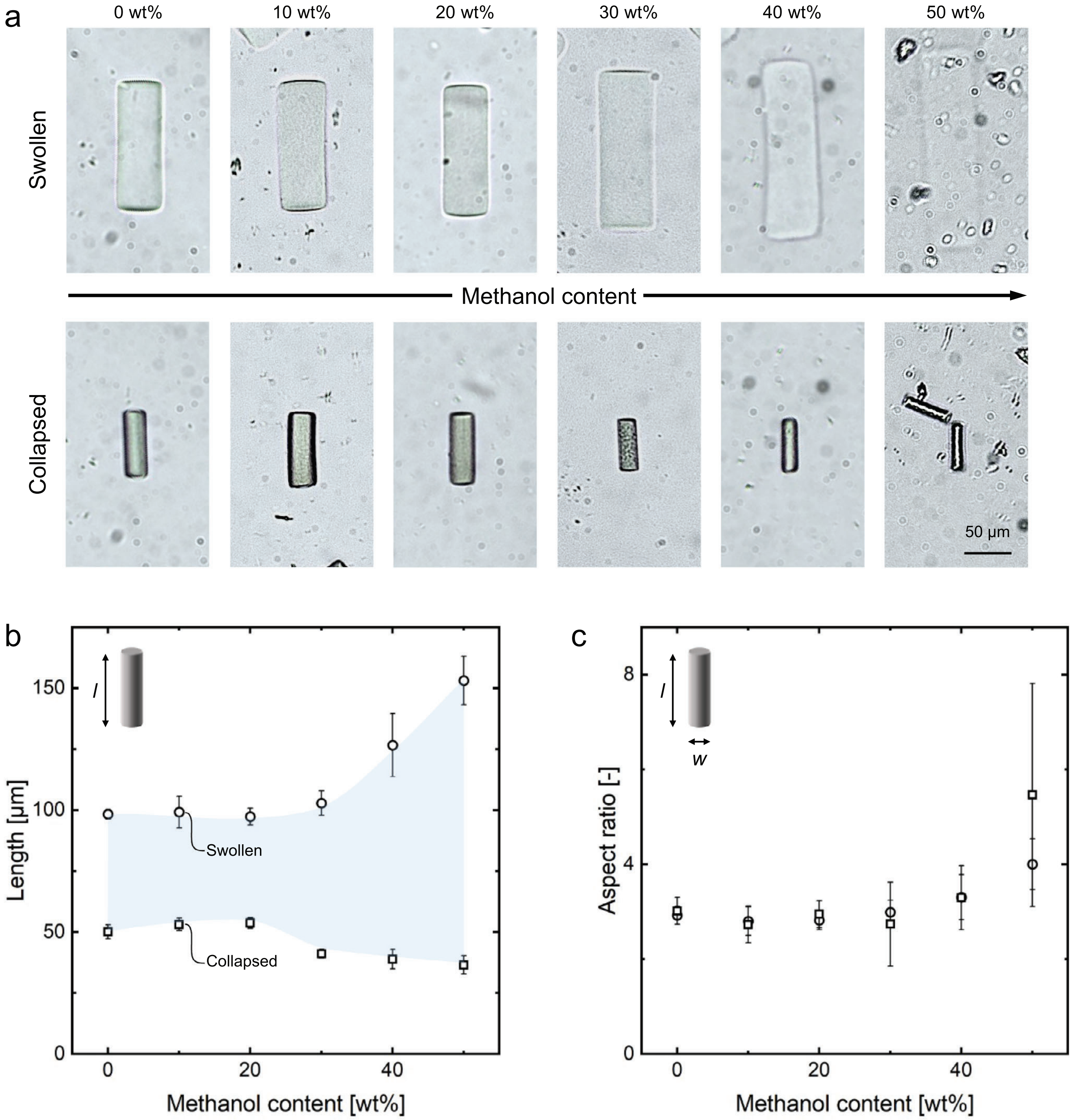

Figure 1. Microgel dimensions. a) Brightfield micrographs of the swollen and collapsed states of exemplary microgels with 0, 20, 30, 40, or 50 wt% methanol. b,c) Length and aspect ratio comparison of microgels that contained different methanol contents in their reaction solutions during microgel fabrication using stop-flow lithography (SFL). Plotted over the methanol content for samples with 0 to 50 wt% methanol in 10 wt% increments, showing the swollen (◎) and collapsed (□) state each. b) Microgel length *l*—the blue shaded area indicates the collapsing degree of the different microgel samples. c) Aspect ratio—length *l* divided by width *w* of the respective microgels.

compared here, as they possess the most significant difference while being fabricated with the same polymerization parameters. The first noticeable difference between the micrographs is their polymeric network. For 40 wt% (compare Figure 2b, left image), this network is thinner than the one of 0 wt% (compare Figure 2a, left image), showing also finer structure. On the contrary, the porosity and the pore sizes of the bulk of both samples are nearly identical, with a porosity of 48.9% and an average pore diameter of 214 ± 120 nm for the 0 wt% and 48.3% and 202 ± 129 nm for the 40 wt% sample (see Section S4,

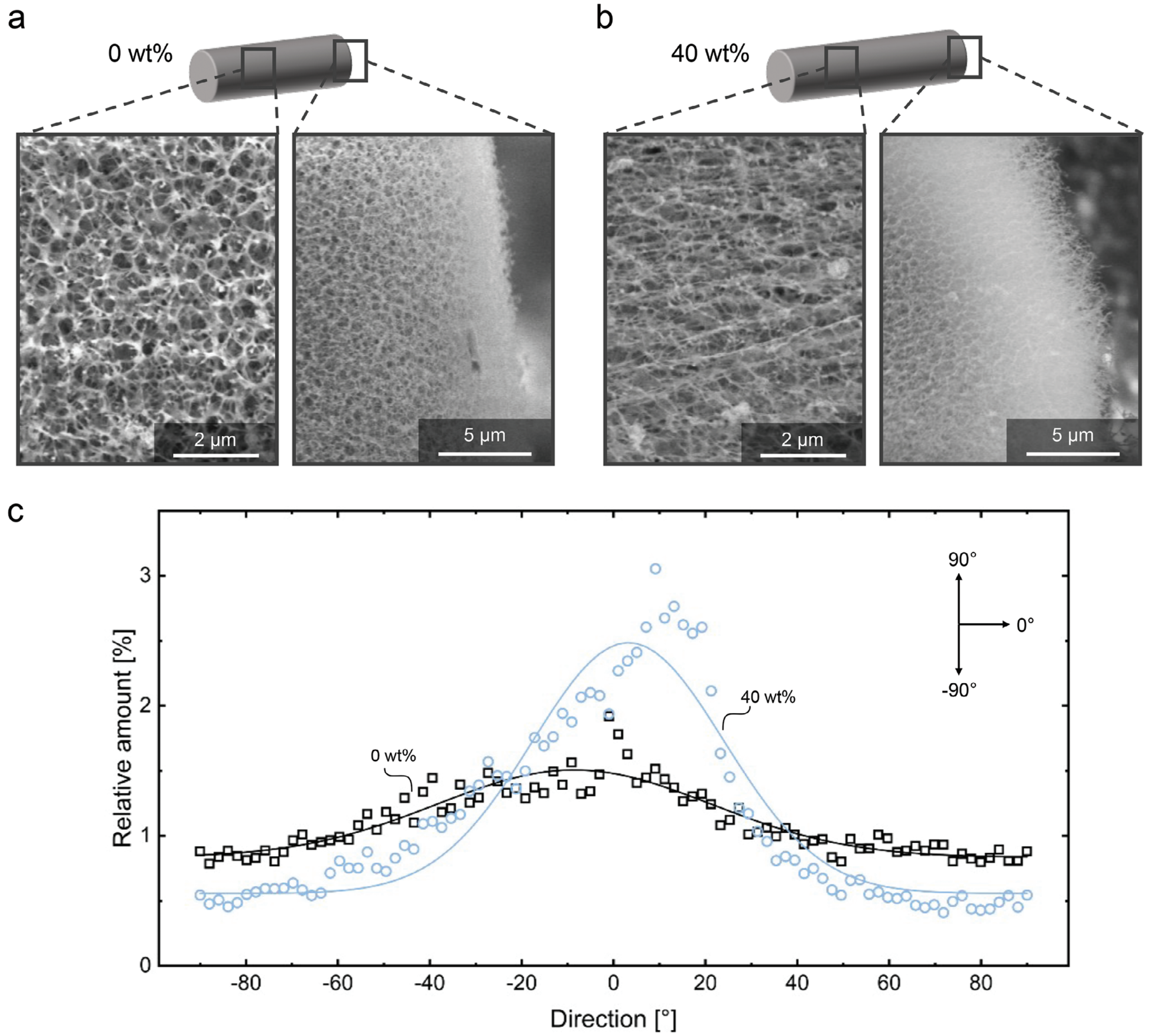

Figure 2. Polymeric structure. CryoFESEM micrographs of microgels in the swollen state fabricated with a) 0 wt% or b) 40 wt% methanol in the reaction solution. Both variants were fabricated with the same conditions despite the methanol content, showing the differences in their polymeric structure. c) Directionality of the polymeric structure with respective Gaussian fit of microgels fabricated with 0 wt% (□, black) or 40 wt% (◎, blue) methanol.

Supporting Information). However, the pores of the 0 wt% microgels are rounder and more evenly distributed, whereas the 40 wt% pores look elongated and stretched along the microgels' longitudinal axis. Since the sphere fitting algorithm that was used to determine the pore diameters assumes spherical pores, the diameters of elliptical pores are given by their minor elliptical pore diameter. As a result, the major diameters of the elliptical pores, which are mainly present for the 40 wt% sample, are probably actually larger than the diameters of the spherical pores of the 0 wt% sample. To confirm this presumable pore elongation of the 40 wt% microgels, the directionality of the polymeric structures of the microgels was measured based on their cryo-FESEM micrographs. Figure 2c shows the relative amount of structures oriented in a certain direction. The arrows (Figure 2c, top left) relate the direction degrees of the graph to the directions within the micrographs. The most prominent direction within the polymeric structure of the 40 wt% sample is around 0°, indicating an orientation of the polymeric structure along the longitudinal axis of the microgels. All other directions are significantly less prominent, confirming the elongation of the polymeric structure of the 40 wt% sample. The 0 wt% sample also shows a slightly increased amount of directed structures at around 0° toward the longitudinal microgel axis. However, the according peak in Figure 2c is comparably low, resulting in an almost flat curve and, thus, little directionality of the 0 wt% sample. A possible explanation for these deviating appearances and the detected elongation of the

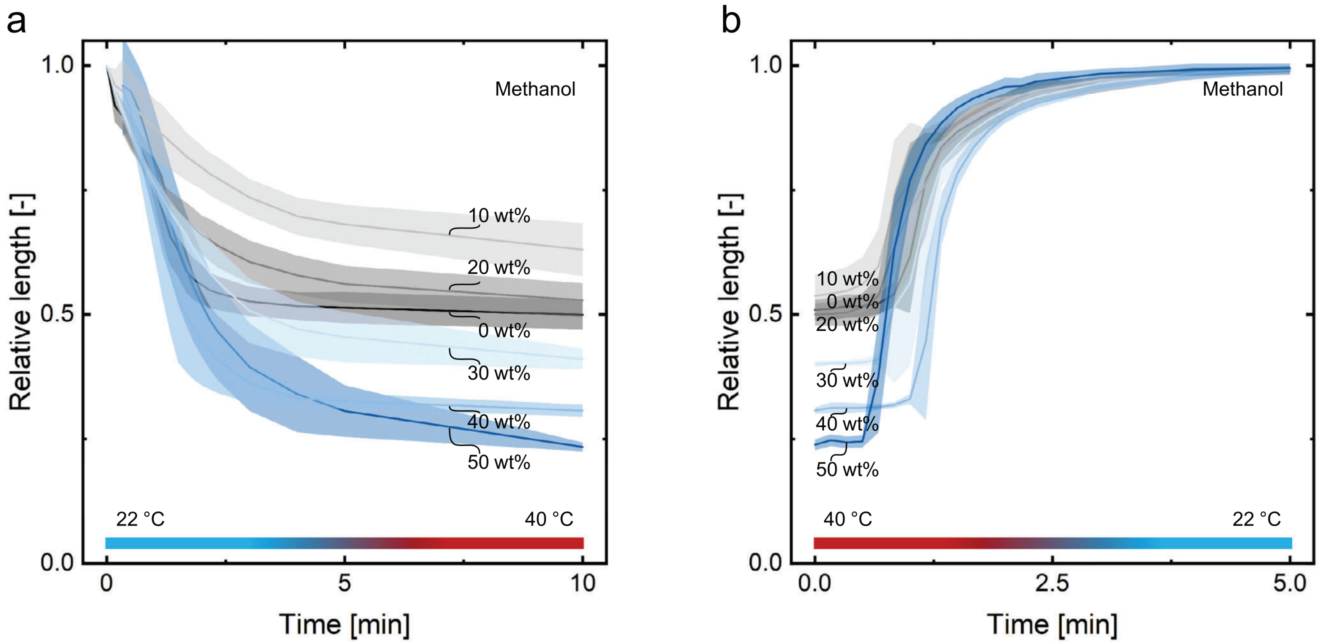

Figure 3. Thermal microgel response. a) Collapsing and b) swelling curves of rod-shaped PNIPAM microgels over time. Temperature-dependent relative lengths of microgels vary by their methanol content (0–50 wt%) during fabrication. Errors are presented as colored regions around the respective curves.

40 wt% sample is the differing microgel lengths despite the same fabrication conditions. Although both samples' lengths were limited by the 80-µm channel height during fabrication, the 40 wt% microgels are 127 ± 13 µm long compared to 98 ± 2 µm of the 0 wt% microgels. Consequently, the microgels elongated in varying degrees subsequent to the exposure-induced polymerization, resulting in the respective polymeric structures. Additionally, the polymer structure at the surface of the microgels significantly differs. The 0 wt% microgels show a distinct and small area with a thinner polymer structure at the surface (compare Figure 2a, right image), whereas the 40 wt% microgels exhibit a noticeably wider area which is more frayed at the border (compare Figure 2b, right image).

Since the microgel dimensions and their polymeric structure depend on the methanol content during fabrication, the presented procedure enables and simplifies the customization of microgel properties to requirements from applications. Thereby, the porous structure of the microgels was tailored without changing the chemical composition of the microgels. Hence, their porosity as the ratio of void volume to total volume remains the same, while their polymeric structure and, as a consequence, their thermal response are significantly altered.

2.4. Time-Dependent Collapsing and Swelling Behavior

In addition to the final swollen and collapsed states as size limits of the microgels, their actual collapsing and swelling behavior is considered. The collapsing and swelling kinetics serve as indicators for the differences in the polymeric structures of the microgels.[17] In **Figure 3a**, the collapsing of these microgels is displayed by the relative microgel length as a function of the experimental time beginning at room temperature and heating up to 40 °C. Not only the extent but also the collapsing kinetics depend significantly on the methanol content during fabrication. For 10 wt% methanol, the velocity is the lowest with 0.22 ± 0.03 µm s^{-1} as maximum collapsing velocity of the sample, while 40 and 50 wt% collapse the fastest with 0.87 ± 0.22 µm s^{-1} and 0.96 ± 0.28 µm s^{-1}, respectively. 0, 20, and 30 wt% show comparable, medium collapsing velocities of 0.41 to 0.61 µm s^{-1} (compare Figure S7a and Table S4, Supporting Information). Furthermore, the velocities are related to the overall collapsing degree of the microgels. Thus, a stronger collapse is equivalent to faster-collapsing microgels. At first, all samples show similar collapsing kinetics, diverging after about 1 min except for 10 wt%, being directly slower. Within the first 2–3 min, the largest changes occur, performing only minor changes in size after this time period. The end states are reached after approximately 10 min, after which the relative microgel lengths show significant differences for different methanol contents as addressed and shown in the prior Section 2.2. The reference with 0 wt% methanol collapses to 51 ± 4% of its prior swollen length, whereas 10 and 20 wt% collapse less. This finding agrees with the observations of previous studies[47,50] about PNIPAM microgels showing their strongest collapse in a methanol-water mixture after fabrication at the same threshold region of 15–20 mol%, which corresponds to 24–31 wt% methanol in water. Above this methanol threshold, a stronger collapse is observed than that of the reference sample. For microgels with a higher methanol content of 30–50 wt%, a correlation is detected between the amount of methanol in the reaction solution and the subsequent collapsing degree and kinetics of the microgels. The more methanol is present during fabrication, the stronger and faster the respective microgels collapse for a threshold above 20 wt% methanol.

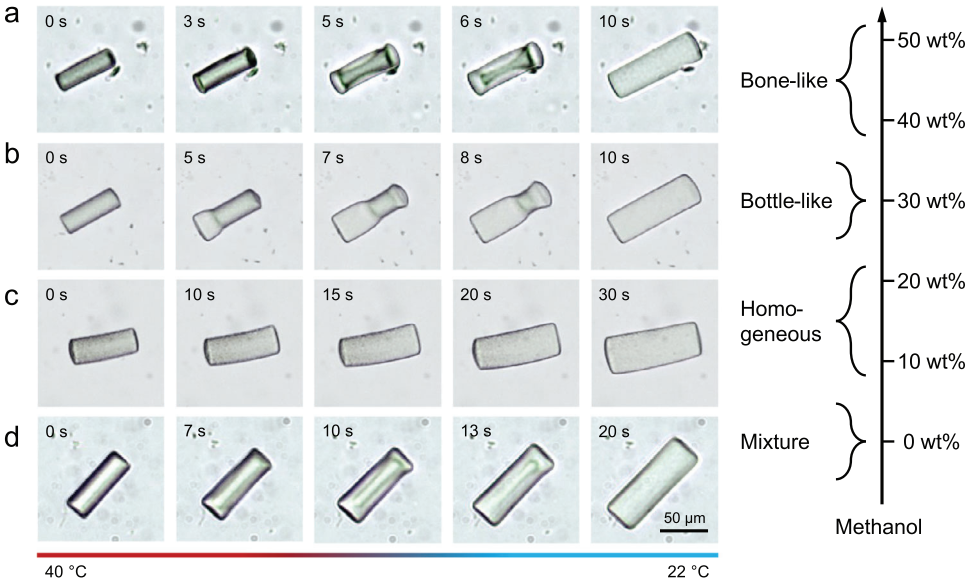

Figure 4. Swelling phenomena. Picture series of swelling processes of microgels fabricated with a) 40 wt%, b) 30 wt%, c) 20 wt%, and d) 0 wt% methanol in the reaction solution. Examples of irregular swelling patterns depend on the methanol content during fabrication.

The swelling behavior of the microgel samples with varying methanol contents during fabrication was investigated by cooling them from 40 °C to 22 °C immediately after collapsing. This swelling is displayed in Figure 3b, considering the relative microgel length as a function of time. Since the actual temperature of the sample is unknown with the setup used, the initial points of the curves cannot be directly related to temperature values. Thus, the initial points could be influenced by the experimental procedure rather than being directly dependent on the temperature and should not be directly compared with each other. However, the relative time dependencies and, hence, the curve shapes are comparable. The shape of all swelling curves is similar, showing an initial resting phase, a rapid swelling phase with comparable swelling velocities, and a constant end phase. Because of the fast swelling kinetics, significant differences in the slope of the swelling curves are difficult to detect. However, the maximum swelling velocities of the samples range from $0.97 \pm 0.31\ \mu m\ s^{-1}$ for 20 wt% to $3.90 \pm 2.10\ \mu m\ s^{-1}$ for 50 wt% (see Figure S7b, Supporting Information). In comparison, the maximum velocities measured during collapsing are significantly lower with $0.22 \pm 0.03\ \mu m\ s^{-1}$ for 10 wt% to $0.96 \pm 0.28\ \mu m\ s^{-1}$ for 50 wt% (compare Table S4, Supporting Information, for all values). Thus, the difference in kinetics during collapsing and swelling of each sample results in a hysteresis. As previously reported for PNIPAM, inter- and intrachain hydrogen bonds may cause this hysteresis. These hydrogen bonds form above the lower critical solution temperature (LCST) during collapsing but dissociate only at temperatures much lower than the LCST during swelling, resulting in a difference of collapsing and swelling in the overall reversible process.[34–36] Due to their different polymeric structures induced by the cononsolvency effect during fabrication, the microgels' thermal responses differ. However, the swelling mechanism remains the same for all observed microgels.

2.5. Swelling Patterns

During the collapsing and swelling, not only the velocities but also the outer contour and shape of the microgels vary. Almost all microgels collapse evenly, retaining their shape over the whole process and displaying a uniform structure throughout the microgel. On the contrary, the swelling is irregular without a consistent shape, but rather a temperature-dependent outer structure. Furthermore, distinct swollen and collapsed regions form within one microgel, resulting in an inner microgel structure. Different irregularities are observed and categorized in swelling patterns, shown in **Figure 4**. The observation of irregular swellings correlates with the swelling mechanism of spherical PNIPAM microgels reported by Cheng et al.[34] in which the microgel shell swells more than its core during the initial swelling phase. Furthermore, swelling is, on average, 3.5 ± 1.1 times faster than collapsing of the respective sample. During swelling, microgel samples with 0, 30, 40, and 50 wt% methanol during fabrication show an irregular swelling, whereas 10 and 20 wt% swell regularly with an even shape expansion in all directions, having regular inner and outer structures irrespective of temperature (Figure 4c). Thus, the swelling behavior is related to the methanol content during microgel fabrication. Moreover, these irregular swellings are related to an increased collapsing degree and higher collapsing and swelling velocities, as the same microgel variants show all these characteristics.

Depending on the methanol content, the swelling phenomena differ. For 40 and 50 wt% methanol, the so-called bone-like swelling is observed (Figure 4a). Swelling starts at the thin sides of the gel and continues even stronger in the middle of the long sides, leading to a bone-like collapsed structure in the middle of the microgel, whereas the surrounding gel network is already swollen. This bone-like structure dissolves in the further swelling process, resulting in the homogeneous initial rod shape of the microgel. This swelling phenomenon can be reasoned by the water and, thus, heat diffusion limitation in the middle of the microgel during swelling, causing a time-delayed swelling in this region. For the 50 wt% microgel sample, not only the swelling reveals irregular microgel patterns, but during its collapse, the bone-like structure was also observed. These irregularities during collapsing might result from the comparatively high collapsing velocity of the 50 wt% microgels which lies in the order of the swelling velocity of the 20 wt% microgels (compare Table S4, Supporting Information).

Another observed swelling phenomenon is called bottle-like swelling and occurs for 30 wt% microgels, which is exemplarily shown in Figure 4b. Here, the thin microgel sides swell time-shifted instead of beginning simultaneously, whereas the swelling process does not proceed from the long sides of the gel. Hence, a bottle-like microgel structure arises with a thin collapsed area between the long sides of the microgel, while both areas related to the thin sides of the microgel are already swollen. The positioning of this collapsed area is likely determined by the focus height of the UV light during microgel fabrication via SFL. According to Dendukuri et al.,[55] the homogeneity in microgel conversion during stop-flow lithography mainly depends on the molar extinction coefficient of the photoinitiator, its concentration, and the channel height due to the light's focus. By contrast, the reactivity difference between the crosslinker and the monomer is less relevant for light-induced polymerization compared to fabrication methods like precipitation polymerization. Thus, homogeneity distributions within microgels fabricated via SFL mainly depend on the focus point applied during fabrication. In this work, the focus is set with respect to a homogeneous but highly focused light over the entire channel height, resulting in minor differences in the lighting power along the channel height and, thus, along the length of the microgels during fabrication. Hence, the occurrence and shift of the collapsed area arise from an increased power as a consequence of the focus and, thus, a denser cross-linking at this point. Even if this effect induced by the SFL process becomes visible in combination with the cononsolvency effect, its influence remains the same for all samples, and thus, these can be compared with regard to the varied methanol content only.

The 0 wt% microgel sample without methanol in the SFL reaction solution shows a mixture of bone-like and bottle-like swelling phenomena (Figure 4d), beginning to swell on one thin microgel side, but results in a collapsed bone-like structure within the microgel. The observed shape effects occur almost exclusively during swelling and are related to the methanol content of the microgel samples. These dependencies fit the previous observations regarding collapsing degree and collapsing and swelling kinetics.

The introduced cononsolvency-driven procedure allows to systematically fabricate anisotropically swelling microgels with domains of varying density and aggregation. Such distinct domains within microgels are of special interest for a variety of applications, such as micrometer-scale targeted folding,[58,59] active swimmers,[60,61] and locally induced contractions for cell growth,[3,62] among others.[2,63–65]

3. Conclusion

In this work, a new fabrication procedure is established to tune the porous structure of thermally responsive rod-shaped PNIPAM microgels. The cononsolvency effect was used during microgel fabrication by replacing water as solvent in the reaction solution with a mixture of water and methanol with different contents of methanol from 0 to 50 wt%. Furthermore, stop-flow lithography (SFL) as a fabrication method enables the realization of microgels of complex shapes in high throughput.

Depending on the methanol content, the microgel characteristics changed. Noticeably, during fabrication, the parameters needed for a successful polymerization and the qualitative stiffness of the microgels varied. Electron microscopy imaging showed deviating polymeric structures between microgels with and without methanol influence. Furthermore, the microgels' thermoresponsiveness was affected by the new fabrication procedure. The microgel length of the swollen state increased with increasing methanol content, whereas the length of the collapsed state decreased. This resulted in an enhanced degree of collapsing with an increase in the methanol content during fabrication. Thereby, the microgel length was more affected than the width, causing elongated microgels with higher aspect ratios, both in the swollen and collapsed states, as the methanol content increased. The collapsing and swelling kinetics depended on the methanol content as well, whereas swelling shape patterns of the microgels occurred, which correlated with the methanol content in the reaction solution during fabrication. For high methanol contents of 40 or 50 wt%, bone-like swelling was observed. 30 wt% microgels showed bottle-like swelling, while samples with low methanol contents of 10 and 20 wt% swelled homogeneously without any pattern. Microgels fabricated without methanol exhibited a mixture of bone-like and bottle-like swelling, showing characteristics of both swelling patterns. These swelling patterns correlate with the swelling velocities observed for the respective samples since homogeneous swelling occurred for the slowest swelling microgels, whereas faster swelling microgels showed varying swelling patterns in correlation with their velocities. Hence, the properties of anisometric PNIPAM microgels changed by the presence of varying methanol contents during fabrication via stop-flow lithography. Their porous structure was modified and consequently, their fabrication parameter, appearance, collapsing degree, and behavior during thermal response varied. This novel procedure enables the development of advanced microgels with tailored porous structure and increased and adjustable responsiveness for medical approaches and cell growth. Thus, injectable scaffolds can be generated with enhanced scaffold properties by applying the presented procedure. Due to the fabrication with SFL, implementing any other complex geometry is straightforward through the design of the mask geometry used in the SFL process. Hence, microgels of complex shape are feasible to further tailor the major pores of these scaffolds in addition to the microgels' porous structure, achieving improved cell infiltration and proliferation.

4. Experimental Section

Reaction Solution Preparation: Each reaction solution contained the monomer *N*-isopropyl acrylamide (NIPAM) (98%, Acros Organics,

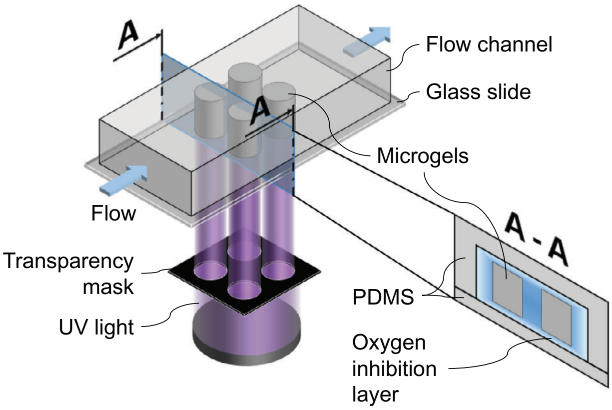

Figure 5. Scheme of the stop-flow lithography (SFL) setup to fabricate anisometric microgels.

recrystallized in hexane (99%, VWR)), the cross-linker N, N'-methylene bisacrylamide (BIS) (99%, Sigma-Aldrich), the initiator lithium phenyl-2,4,6-trimethyl-benzoyl phosphinate (LAP) (⩾ 95%, Sigma-Aldrich), and a solvent solution. The solvent solutions contained the surfactant sodium dodecyl sulfate (SDS) (99%, AppliChem), water (HiPerSolv CHROMANORM, VWR), and methanol (⩾ 99.5%, Carl Roth).

For the preparation of the standard reaction solution without methanol,[4] SDS (40 mmol L^{-1}) was dissolved in water, resulting in the solvent solution. The monomer (20 wt%), the cross-linker (2 wt%), and the initiator (1 wt%) were weight out into separate vials each. Afterward, the solvent solution (77 wt%) was added to the cross-linker and mixed thoroughly before being transferred to the vial with the monomer. After all components dissolved, this mixture was added to the initiator as the last component, mixed, and centrifuged to remove any air bubbles that appeared during solution preparation. For samples with methanol, the solvent solution was adapted but its volume was maintained to keep the mass concentration of monomer, cross-linker, and initiator constant. Depending on the sample variant, the water content was partly replaced with methanol in the respective amount (0, 10, 20, 30, 40, or 50 wt% of the solvent solution). Thus, the cononsolvency effect was induced during the microgel fabrication to adapt the porous structure and softness of the microgels.

Microgel Fabrication using SFL: Stop-flow lithography (SFL) was used to fabricate the microgel variants. The basic principle of SFL is established in previous works[4,51,55] and visualized in **Figure 5**, whereas Wolff et al.[4] listed the individual components of the self-constructed setup used in this work. The production of the microfluidic chips out of polydimethylsiloxane (PDMS) was performed according to previous work.[66] The glass slide (VWR, 52 × 76 × 1 mm) was coated with PDMS to enable oxygen diffusion from the bottom of the chip into the channel (15-mm length, 900-µm width, 80-µm height) as well as from the top. For the microgel fabrication in this work, a transparency mask with circular patterns (200-µm diameter, 400-µm distance to each other) was used, leading to microgel rods (37-µm diameter, 80-µm length). To ensure an equivalent comparison between microgel variants with different methanol contents, every parameter influencing the fabrication except for the methanol content was held constant. All microgel variants were fabricated with the same radiant flux (193 mW, 365 nm). However, as explained in Section 2.1, the 50 wt% methanol sample required a longer exposure time (425 ms) compared to all other samples (325 ms) to achieve stable microgels.

Prior to subsequent investigations, all fabricated microgel samples were purified by using dialysis. Therefore, the sample was filled in a cellulose dialysis membrane tube (Zellutrans, MWCO: 12–14 kDa, 25-mm flat width, 20-µm wall thickness, Carl Roth GmbH) and inserted in deionized water (10 L, 2 × 24 h) to exchange the reaction solution. Until analysis, the purified samples were stored at 4 °C to avoid arising biological impurities.

Temperature-Induced Collapsing and Swelling Experiments: The thermal response of the microgels was investigated by heating them (from 22 to 40 °C) and then allowing them to cool again (to 22 °C). During the analysis, the volume phase transition temperature (VPTT) of the PNIPAM microgels of 32 °C[40,47] was exceeded. Therefore, the microgel sample was warmed up (30 min) to room temperature (22 °C) prior to the analysis. Afterward, the sample (20 µL) was inserted in a self-constructed PDMS chamber which was subsequently filled up with water (HiPerSolv CHROMANORM, VWR) (40 µL). The filled chamber was covered with a glass slide to prevent the solvent from evaporating. After sedimentation of the microgels (20 min), the sample was placed on a preheated (40 °C) heating stage (H601-M-frame-glass, Okolab) that was attached to an inverse light microscope (DM IL LED, Leica). Immediately after the sample heating (40 °C, 20 min), the sample was cooled down (22 °C, 20 min) by lowering the temperature of the heating stage without active cooling. A sketch of the experimental setup is shown in Figure S2 (Supporting Information). The experiments were repeated for three subsamples of every microgel variant with varying methanol content during fabrication. From each subsample, four randomly selected microgels were evaluated, resulting in a total analyzed amount of twelve microgels per methanol content. Microgel length and width were measured (ImageJ, version 1.53a) at defined time points (every 10 s within the first 2.5 min and after 3, 4, 5, 10, and 20 min) from micrographs taken periodically (1 fps) during heating and cooling.

Analysis of the Polymeric Microgel Structures: For the investigation of the polymeric structure of the microgels, a water drop containing swollen microgels was frozen in liquid ethane (1 min) and stored until imaging in liquid nitrogen (cryo). Using a field emission electron microscope (FESEM) (S4800, Hitachi), the frozen sample drop was cut to visualize the microgels' polymer structure and cross sections and was sublimated (2 × 20 min, −80 °C) before being imaged (1–3 kV, 1 µA). In addition to the qualitatively visual observation, the FESEM micrographs were evaluated to quantitatively determine the properties of the polymeric structure of the microgels. Therefore, a tailored Python script was used. To calculate the porosity of the microgels, all pixels representing pores in the binarized cryo FESEM micrographs were counted. Furthermore, the pore diameter distributions and mean diameters were determined by using a sphere fitting algorithm.[67] The directionality of the polymeric structures was determined via a plug-in of the software Fiji (version 2.15.0) as a distribution of ImageJ. Further information regarding the software-based evaluation of the polymeric structure is given in Section S4 (Supporting Information).

Supporting Information

Supporting Information is available from the Wiley Online Library or from the author.

Acknowledgements

This work was financially supported by the Deutsche Forschungsgemeinschaft (DFG) within the SFB 985 "Functional Microgels and Microgel Systems" project B5 and by the Werner Siemens Foundation (Project TriggerINK). M.W. acknowledges DFG funding through the Gottfried Wilhelm Leibniz Award 2019 (WE 4678/12-1) and the Alexander-von-Humboldt Foundation. The authors thank Dr.-Ing. Daniel Bell and Dr.-Ing. Arne Lüken for their input and fruitful discussions, Dr.-Ing. Abdolrahman Omidinia Anarkoli for conducting the cryo FESEM micrographs, and Florian Wiesner for supporting with the polymeric structure evaluation.

Open access funding enabled and organized by Projekt DEAL.

Conflict of Interest

The authors declare no conflict of interest.

Author Contributions

Lea Steinbeck: Conceptualization, Data Curation, Formal Analysis, Investigation, Methodology, Project Administration, Supervision, Validation, Vi-

sualization, Writing - Original Draft, Writing - Review & Editing. Hanna J. M. Wolff: Conceptualization, Data Curation, Methodology, Project Administration, Supervision, Validation. Maximilian Middeldorf: Investigation, Formal Analysis, Methodology. Matthias Wessling, John Linkhorst: Conceptualization, Funding Acquisition, Project Administration, Resources, Supervision, Writing - Review & Editing.

Data Availability Statement

The data that support the findings of this study are available from the corresponding author upon reasonable request.

Keywords

anisometric microgels, cononsolvency, PNIPAM, porosity, thermal response

Received: December 13, 2023
Revised: February 26, 2024
Published online: March 23, 2024

---

[1] M. Karg, A. Pich, T. Hellweg, T. Hoare, L. A. Lyon, J. J. Crassous, D. Suzuki, R. A. Gumerov, S. Schneider, Igor. I. Potemkin, W. Richtering, *Langmuir* **2019**, *35*, 6231.
[2] B. Garcia-Pinel, A. Ortega-Rodríguez, C. Porras-Alcalá, L. Cabeza, R. Contreras-Cáceres, R. Ortiz, A. Díaz, A. Moscoso, F. Sarabia, J. Prados, J. M. López-Romero, C. Melguizo, *Artif. Cells Nanomed. Biotechnol.* **2020**, *48*, 1022.
[3] S. Schmidt, M. Zeiser, T. Hellweg, C. Duschl, A. Fery, H. Möhwald, *Adv. Funct. Mater.* **2010**, *20*, 3235.
[4] H. J. M. Wolff, J. Linkhorst, T. Göttlich, J. Savinsky, A. J. D. Krüger, L. De Laporte, M. Wessling, *Lab Chip* **2020**, *20*, 285.
[5] A. Scotti, M. F. Schulte, C. G. Lopez, J. J. Crassous, S. Bochenek, W. Richtering, *Chem. Rev.* **2022**, *122*, 11675.
[6] Q. Feng, K. Wei, S. Lin, Z. Xu, Y. Sun, P. Shi, G. Li, L. Bian, *Biomaterials* **2016**, *101*, 217.
[7] D. R. Griffin, W. M. Weaver, P. O. Scumpia, D. Di Carlo, T. Segura, *Nat. Mater.* **2015**, *14*, 737.
[8] M. Liu, X. Zeng, C. Ma, H. Yi, Z. Ali, X. Mou, S. Li, Y. Deng, N. He, *Bone Res.* **2017**, *5*, 1.
[9] J. P. Newsom, K. A. Payne, M. D. Krebs, *Acta Biomater.* **2019**, *88*, 32.
[10] H. Wang, J. Zhou, Z. Liu, C. Wang, *J. Cell. Mol. Med.* **2010**, *14*, 1044.
[11] M. S. Riederer, B. D. Requist, K. A. Payne, J. D. Way, M. D. Krebs, *Carbohydr. Polym.* **2016**, *152*, 792.
[12] L. P. B. Guerzoni, J. C. Rose, D. B. Gehlen, A. Jans, T. Haraszti, M. Wessling, A. J. C. Kuehne, L. De Laporte, *Small* **2019**, *15*, 1900692.
[13] S. Babu, F. Albertino, A. Omidinia Anarkoli, L. De Laporte, *Adv. Healthcare Mater.* **2021**, *10*, 2002221.
[14] D. J. Griffon, M. R. Sedighi, D. V. Schaeffer, J. A. Eurell, A. L. Johnson, *Acta Biomater.* **2006**, *2*, 313.
[15] N. Hübsch, E. Lippens, K. Lee, M. Mehta, S. T. Koshy, M. C. Darnell, R. M. Desai, C. M. Madl, M. Xu, X. Zhao, O. Chaudhuri, C. Verbeke, W. S. Kim, K. Alim, A. Mammoto, D. E. Ingber, G. N. Duda, D. J. Mooney, *Nat. Mater.* **2015**, *14*, 1269.
[16] D. Rommel, M. Mork, S. Vedaraman, C. Bastard, L. P. B. Guerzoni, Y. Kittel, R. Vinokur, N. Born, T. Haraszti, L. De Laporte, *Adv. Sci.* **2022**, *9*, 2103554.
[17] C.-L. Mou, X.-J. Ju, L. Zhang, R. Xie, W. Wang, N.-N. Deng, J. Wei, Q. Chen, L.-Y. Chu, *Langmuir* **2014**, *30*, 1455.
[18] D. J. Bell, D. Roedder, M. Wessling, *ACS Appl. Polym. Mater.* **2020**, *2*, 932.
[19] J. Wan, A. Bick, M. Sullivan, H. A. Stone, *Adv. Mater.* **2008**, *20*, 3314.
[20] W. J. Duncanson, M. Zieringer, O. Wagner, J. N. Wilking, A. Abbaspourrad, R. Haag, D. A. Weitz, *Soft Matter* **2012**, *8*, 10636.
[21] S. B. Rauer, D. J. Bell, P. Jain, K. Rahimi, D. Felder, J. Linkhorst, M. Wessling, *Adv. Mater. Technol.* **2022**, *7*, 2100836.
[22] C. S. Biswas, V. K. Patel, N. K. Vishwakarma, A. K. Mishra, B. Ray, *J. Appl. Polym. Sci.* **2011**, *121*, 2422.
[23] C. S. Biswas, V. K. Patel, N. K. Vishwakarma, A. K. Mishra, R. Bhimireddi, R. Rai, B. Ray, *J. Appl. Polym. Sci.* **2012**, *125*, 2000.
[24] B. V. Slaughter, S. S. Khurshid, O. Z. Fisher, A. Khademhosseini, N. A. Peppas, *Adv. Mater.* **2009**, *21*, 3307.
[25] Y. Wen, Y. Liu, H. Zhang, M. Zou, D. Yan, D. Chen, Y. Zhao, *Nanoscale* **2019**, *11*, 2687.
[26] P. A. Janmey, D. A. Fletcher, C. A. Reinhart-King, *Physiol. Rev.* **2020**, *100*, 695.
[27] M. J. Paszek, N. Zahir, K. R. Johnson, J. N. Lakins, G. I. Rozenberg, A. Gefen, C. A. Reinhart-King, S. S. Margulies, M. Dembo, D. Boettiger, D. A. Hammer, V. M. Weaver, *Cancer Cell* **2005**, *8*, 241.
[28] S. Saxena, M. W. Spears, H. Yoshida, J. C. Gaulding, A. J. García, L. A. Lyon, *Soft Matter* **2014**, *10*, 1356.
[29] L.-Y. Chu, J.-W. Kim, R. K. Shah, D. A. Weitz, *Adv. Funct. Mater.* **2007**, *17*, 3499.
[30] F. A. Plamper, W. Richtering, *Acc. Chem. Res.* **2017**, *50*, 131.
[31] X. Sui, Q. Chen, M. A. Hempenius, G. J. Vancso, *Small* **2011**, *7*, 1440.
[32] J. D. Humphrey, E. R. Dufresne, M. A. Schwartz, *Nat. Rev. Mol. Cell Biol.* **2014**, *15*, 802.
[33] R. Foudazi, R. Zowada, I. Manas-Zloczower, D. L. Feke, *Langmuir* **2023**, *39*, 2092.
[34] H. Cheng, L. Shen, C. Wu, *Macromolecules* **2006**, *39*, 2325.
[35] Y. Lu, K. Zhou, Y. Ding, G. Zhang, C. Wu, *PCCP Phys. Chem. Chem. Phys.* **2010**, *12*, 3188.
[36] B. Sun, Y. Lin, P. Wu, H. W. Siesler, *Macromolecules* **2008**, *41*, 1512.
[37] B. Sierra-Martin, J. R. Retama, M. Laurenti, A. F. Barbero, E. L. Cabarcos, *Adv. Colloid Interface Sci.* **2014**, *205*, 113.
[38] H. Bachman, A. C. Brown, K. C. Clarke, K. S. Dhada, A. Douglas, C. E. Hansen, E. Herman, J. S. Hyatt, P. Kodlekere, Z. Meng, S. Saxena, M. W. Spears Jr, N. Welsch, L. A. Lyon, *Soft Matter* **2015**, *11*, 2018.
[39] M. Y. Hwang, S. G. Kim, H. S. Lee, S. J. Muller, *Soft Matter* **2017**, *13*, 5785.
[40] A. Chetty, J. Kovács, Z. Sulyok, Á. Mészáros, J. Fekete, A. Domján, A. Szilágyi, V. Vargha, *eXPRESS Polym. Lett.* **2013**, *7*, 95.
[41] A. J. Krüger, O. Bakirman, L. P. Guerzoni, A. Jans, D. B. Gehlen, D. Rommel, T. Haraszti, A. J. Kuehne, L. De Laporte, *Adv. Mater.* **2019**, *31*, 1903668.
[42] S. Bulut, S.-H. Jung, T. Bissing, F. Schmitt, M. Bund, S. Braun, A. Pich, *Small* **2023**, 2303783.
[43] Z. Gan, H. Liu, Y. Wang, T. Tao, M. Zhao, J. Qin, *Adv. Mater. Technol.* **2023**, *8*, 2201102.
[44] E. Sulu, C. S. Biswas, F. J. Stadler, B. Hazer, *J. Porous Mater.* **2017**, *24*, 389.
[45] F. Tanaka, T. Koga, F. M. Winnik, *Phys. Rev. Lett.* **2008**, *101*, 028302.
[46] S. Bharadwaj, B.-J. Niebuur, K. Nothdurft, W. Richtering, N. F. A. van der Vegt, C. M. Papadakis, *Soft Matter* **2022**, *18*, 2884.
[47] C. Scherzinger, A. Schwarz, A. Bardow, K. Leonhard, W. Richtering, *Curr. Opin. Colloid Interface Sci.* **2014**, *19*, 84.
[48] J. Dudowicz, K. F. Freed, J. F. Douglas, *J. Chem. Phys.* **2015**, *143*, 131101.
[49] H. Yong, J.-U. Sommer, *Macromolecules* **2022**, *55*, 11034.
[50] K. Nothdurft, D. H. Müller, T. Brands, A. Bardow, W. Richtering, *PCCP Phys. Chem. Chem. Phys.* **2019**, *21*, 22811.
[51] D. Dendukuri, S. S. Gu, D. C. Pregibon, T. A. Hatton, P. S. Doyle, *Lab Chip* **2007**, *7*, 818.

[52] K. W. Bong, J. Lee, P. S. Doyle, *Lab Chip* **2014**, *14*, 4680.

[53] K. W. Bong, D. C. Pregibon, P. S. Doyle, *Lab Chip* **2009**, *9*, 863.

[54] K. S. Paulsen, D. Di Carlo, A. J. Chung, *Nat. Commun.* **2015**, *6*, 6976.

[55] D. Dendukuri, P. Panda, R. Haghgooie, J. M. Kim, T. A. Hatton, P. S. Doyle, *Macromolecules* **2008**, *41*, 8547.

[56] E. Izak-Nau, D. E. Demco, S. Braun, C. Baumann, A. Pich, R. Göstl, *ACS Appl. Polym. Mater.* **2020**, *2*, 1682.

[57] J. B. Thorne, G. J. Vine, M. J. Snowden, *Colloid Polym. Sci.* **2011**, *289*, 625.

[58] J. Yin, W. Fan, Z. Xu, J. Duan, Y. Xia, Z. Nie, K. Sui, *Small* **2022**, *18*, 2104440.

[59] H. Zhang, A. Mourran, M. Möller, *Nano Lett.* **2017**, *17*, 2010.

[60] A. Mourran, O. Jung, R. Vinokur, M. Möller, *Eur. Phys. J. E* **2021**, *44*, 79.

[61] C. Wischnewski, J. Kierfeld, *Soft Matter* **2020**, *16*, 7088.

[62] Y. Chandorkar, A. Castro Nava, S. Schweizerhof, M. Van Dongen, T. Haraszti, J. Köhler, H. Zhang, R. Windoffer, A. Mourran, M. Möller, L. De Laporte, *Nat. Commun.* **2019**, *10*, 4027.

[63] H. Zhang, X. Guo, J. Wu, D. Fang, Y. Zhang, *Sci. Adv.* **2018**, *4*, eaar8535.

[64] R. Chen, J. Shi, C. Liu, J. Li, S. Cao, *Adv. Compos. Hybrid Mater.* **2022**, *5*, 2223.

[65] B. Xue, V. Kozlovskaya, E. Kharlampieva, *J. Mater. Chem. B* **2017**, *5*, 9.

[66] L. Steinbeck, D. L. Braunmiller, H. J. Wolff, V. Hüttche, J. Wang, M. Wessling, J. J. Crassous, J. Linkhorst, *Adv. Mater. Technol.* **2023**, *8*, 2300044.

[67] M. Sabharwal, L. Pant, A. Putz, D. Susac, J. Jankovic, M. Secanell, *Fuel Cells* **2016**, *16*, 734.